

Dynamical excitation and anelastic relaxation of ferroelastic domain walls in LaAlO₃

Richard J. Harrison,* Simon A. T. Redfern, and Ekhard K. H. Salje

Department of Earth Sciences, University of Cambridge, Downing Street, Cambridge CB2 3EQ, United Kingdom

(Received 16 September 2003; published 1 April 2004)

The ferroelastic domain processes responsible for low-frequency anelasticity in LaAlO₃ have been investigated using dynamical mechanical analysis in three-point bend geometry combined with *in situ* optical observations under dynamic stress at high temperature. Transformations in the types of collective motion of domain walls have been observed optically. For low temperatures and small forces, the anelastic response is dominated by rapid advancement/retraction of combs of {100}_{pc} needle domains. At higher temperatures, lateral translation/rotation of {110}_{pc} twins also contributes to the response. Needle tips are pinned by a broad range of potentials, such that the ratio of mobile to static needle tips increases steadily with increasing temperature. For large forces, three distinct peaks in the relaxation spectrum can be resolved. A small low-temperature peak in the mechanical loss is attributed to the rapid saturation of weakly pinned needles. The dominant intermediate-temperature loss peak is attributed to the gradual relaxation of the comb as a whole. A third high-temperature loss peak occurs at the end of the domain-freezing regime and the beginning of the saturation regime. Activation energies for domain-wall motion of 95, 85, and 86 kJ/mol were determined for samples subjected to low, intermediate, and high forces, respectively. Cole-Cole plots of the response at small forces show a linear section at intermediate frequency and a depressed semicircle at low frequency. The semicircular portion is very well described by the Cole-Cole equation with a broadening exponent μ . Physically, this model corresponds to a Debye-like relaxation process with a distribution of activation energies (domain-sliding regime). The broadening of the relaxation peak is a function of temperature, with μ decreasing from 0.7 at 130 °C to 0.5 at 205 °C. This corresponds to an increase in the full width at half maximum of the activation-energy distribution from 9 to 21 kJ/mol. Fits to the entire data set suggest a parabolic temperature dependence of μ with maximum at ~120 °C. A number of physical processes are suggested to explain this phenomenon. The linear portion of the Cole-Cole plots provides evidence for a dynamic “transition” between the domain-sliding and thermally activated creep regimes with increasing frequency.

DOI: 10.1103/PhysRevB.69.144101

PACS number(s): 62.40.+i, 81.40.Jj, 91.60.-x

INTRODUCTION

The dynamic response of ferroelastic domain walls to an alternating applied stress at frequencies in the region of 1 Hz has recently been the subject of intense investigation, due to the ability of mobile domain walls to modify the seismic signature of ferroelastic minerals.^{1–3} The low-frequency mechanical properties of ferroelastic materials are found to be highly sensitive to the presence of twins.^{4,5} Typically, one can identify three distinct regimes of mechanical behavior as a function of temperature. The paraelastic regime ($T > T_c$) corresponds to the stability field of the high-symmetry phase. The material contains no twins and the mechanical response measured at low frequencies is essentially equal to the instantaneous elastic response of the lattice. The superelastic regime ($T < T_c$) corresponds to the stability field of the low-symmetry phase. Transformation twins form spontaneously below T_c , and the mechanical response is the sum of the instantaneous (on the time scale of this experiment) elastic response of the lattice and a time-dependent (i.e., anelastic) response due to thermally activated displacement of domain walls. This leads to an enormous reduction in Young’s modulus (by up to a factor of ten) and an increase in internal friction (i.e., the energy dissipated per cycle). A further domain-freezing regime ($T < T_f$) is caused by a reduction in domain-wall mobility on cooling. It is characterized by a rapid increase in storage modulus and a pronounced peak in internal friction. The domain-freezing regime is of great in-

terest, because it contains information about the wall-defect, wall-wall, and wall-surface interactions controlling domain-wall mobility.⁶ Such information is required if the influence of domain walls on the mechanical properties of solids at high P and T is to be inferred from experiments performed at atmospheric pressure. Here we present an investigation of the domain-freezing regime in single-crystal LaAlO₃, using a combination of dynamical mechanical analysis (DMA) and *in situ* optical observation. Variations in internal friction are mapped out in detail throughout temperature-frequency-force space. The experiments allow us to identify different modes of anelastic response and to determine their corresponding distributions of activation energies.

BACKGROUND AND THEORY**Anelastic relaxation**

The ferroelastic domain-freezing regime is well described by the theory of anelastic relaxation.⁷ When a constant stress σ_0 is applied to an anelastic material, the strain $\varepsilon(t)$ develops over a characteristic relaxation time τ . The ansatz for the response is usually an exponential decay:

$$J(t) = \frac{\varepsilon(t)}{\sigma_0} = J_U + \Delta J(1 - e^{-t/\tau}), \quad (1)$$

where $J(t)$ is the total elastic compliance, J_U is the unrelaxed compliance (i.e., the instantaneous elastic response of

the lattice), and ΔJ is the anelastic contribution to the compliance. The time dependence arises due to coupling between the macroscopic strain and a thermally activated relaxation process (which in this case involves the depinning and displacement of ferroelastic domain walls). Subjected to an alternating stress $\sigma = \sigma_0 e^{i\omega t}$, the strain lags behind the stress by a phase angle δ , such that $\varepsilon = \varepsilon_0 e^{i(\omega t - \delta)}$. The dynamic compliance is defined as

$$J^*(\omega) = \frac{\varepsilon}{\sigma} = \frac{\varepsilon_0}{\sigma_0} e^{-i\delta} = J_1(\omega) - iJ_2(\omega). \quad (2)$$

The reciprocal of the dynamic compliance is the dynamic Young's modulus:

$$M^*(\omega) = J^*(\omega)^{-1} = \frac{\sigma}{\varepsilon} = \frac{\sigma_0}{\varepsilon_0} e^{i\delta} = M_1(\omega) + iM_2(\omega). \quad (3)$$

The real part $M_1 = \sigma_0/\varepsilon_0 \cos \delta$ is termed the storage modulus and the imaginary part $M_2 = \sigma_0/\varepsilon_0 \sin \delta$ is termed the loss modulus. The ratio $M_2/M_1 = \tan \delta$ is a measure of the energy dissipated per cycle due to internal friction (often referred to as the inverse quality factor Q^{-1}). The dynamic response functions J_1 and J_2 [Eq. (2)] are related to M_1 and $\tan \delta$ via

$$J_1 = [M_1(1 + \tan^2 \delta)]^{-1}, \quad J_2 = \frac{M_2}{|M^*|^2}. \quad (4)$$

The frequency dependence of J^* , J_1 , and J_2 follows directly from the exponential decay in Eq. (1) as a Debye function:

$$\begin{aligned} J^*(\omega) &= J_U + \Delta J \frac{1}{1 + i\omega\tau}, \\ J_1(\omega) &= J_U + \frac{\Delta J}{1 + \omega^2\tau^2}, \\ J_2(\omega) &= \Delta J \frac{\omega\tau}{1 + \omega^2\tau^2}. \end{aligned} \quad (5)$$

The relaxation time is generally taken as a thermally activated quantity with

$$\tau = \tau_0 \exp(E/RT), \quad (6)$$

where E is an activation energy and T is the temperature. Hence, the relaxation process can be studied either as a function of frequency at constant temperature or as a function of temperature at constant frequency. Whereas the former approach is commonly used in dielectric spectroscopy, the latter approach is most practical in mechanical spectroscopy due to instrumental limitations.

Phase transitions and twinning in LaAlO₃

Above 550 °C, LaAlO₃ has the cubic perovskite structure with space group $Pm\bar{3}m$ and lattice parameter $a_{\text{cubic}} \sim 3.79$ Å. Below 550 °C it undergoes an improper ferroelastic phase transition to the rhombohedral subgroup $R\bar{3}c$,

driven by rotation of the AlO₆ octahedra about one of the cubic threefold symmetry axes. To index domain walls and define the crystallographic orientation of the sample, we define a pseudocubic unit cell with rhombohedral shape ($a_{\text{pc}} = b_{\text{pc}} = c_{\text{pc}} \sim 3.79$ Å and $\alpha_{\text{pc}} = \beta_{\text{pc}} = \gamma_{\text{pc}} \neq 90^\circ$) that is directly comparable in size and orientation to the high-temperature cubic unit cell. The lattice parameters and twin angle have been determined in previous studies as a function of temperature.⁸⁻¹³ The thermodynamic character of the transition is, within experimental resolution, second order.

The crystallography of the twin microstructure in LaAlO₃ is described by Bueble *et al.*,⁸ Bueble and Schmahl,¹⁴ and Harrison *et al.*³ There are four pure twin domain states, corresponding to the four triad axes about which octahedral rotation can occur. For each pair of domains there are two orientations of domain wall, one of the form $\{100\}_{\text{pc}}$ and one of the form $\{110\}_{\text{pc}}$. When all four domain states occur in a single region, a characteristic ‘‘chevron’’ microstructure forms.⁸ The four domains within a chevron are separated by three mutually compatible domain walls (two of the form $\{110\}_{\text{pc}}$ and one of the form $\{100\}_{\text{pc}}$) intersecting along a common $\langle 100 \rangle_{\text{pc}}$ direction. There are six distinguishable chevron orientations.^{3,14} An optical micrograph of the crystal used in this study is shown in Fig. 1. The central region combines $(100)_{\text{pc}}$ walls perpendicular to the surface with $(101)_{\text{pc}}$ and $(10\bar{1})_{\text{pc}}$ walls inclined at 45° to the surface. The inclined walls are easily identified by bands of optical interference fringes arising from the variation in retardation. Although the three domain walls within a given chevron are mutually compatible, allowing a stress-free intergrowth of the four domain states, the six chevrons are not mutually compatible with each other, and high lattice strains occur at the incompatible boundary between regions containing different chevron orientations. On annealing, the high strain at the boundary is partially relieved by the formation of needle twins at the points where $\{100\}_{\text{pc}}$ domain walls intersect (several examples of this behavior can be seen at the top and bottom of Fig. 1).

EXPERIMENTAL DETAILS

The sample studied here was a single crystal of LaAlO₃ with length 9.5 mm, width 1.96 mm, and thickness 0.52 mm (Crystal GmbH, Berlin). The surface of the sample was parallel to $(001)_{\text{pc}}$ and its length parallel to $[110]_{\text{pc}}$. Mechanical properties were measured using a Perkin-Elmer dynamical mechanical analyser (DMA-7) operating in three-point bend geometry. The sample was suspended on two knife-edges, 5 mm apart. A force is applied from above via a third knife-edge located halfway between the supporting knives. The total force is the sum of a static component F_S and a dynamic component with amplitude F_D and frequency f (where $\omega = 2\pi f$). The amplitude of deflection (u_D) and phase lag (δ) are measured via electromagnetic inductive coupling with resolutions of $\Delta u_D \sim 10$ nm and $\Delta \delta \sim 0.1^\circ$, respectively. The dynamic Young's modulus is then

$$M^*(\omega) = \frac{l^3}{4t^3w} \frac{F_D}{u_D} \exp(i\delta), \quad (7)$$

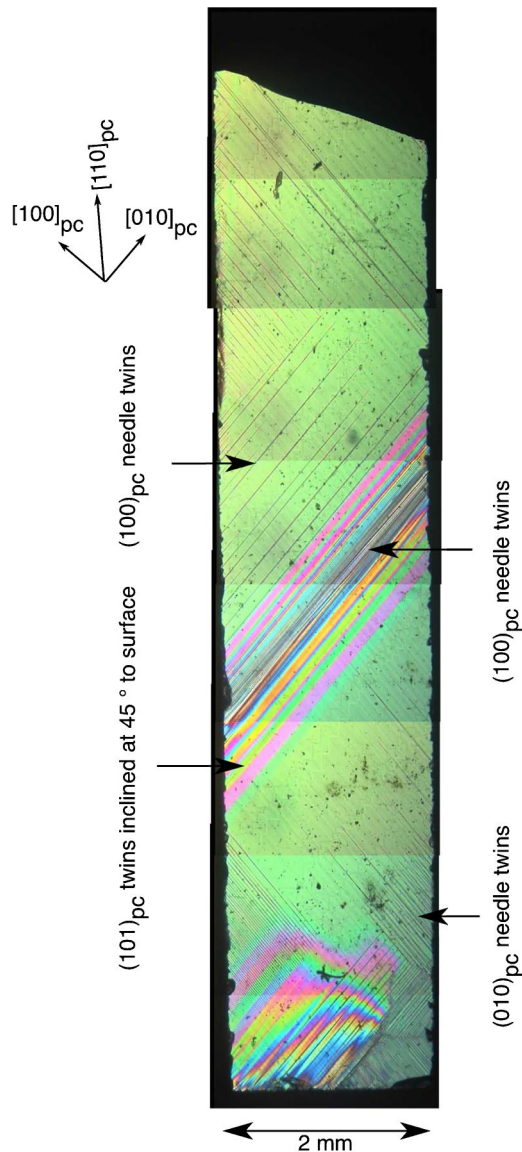


FIG. 1. (Color online) Single-crystal LaAlO_3 sample used for DMA measurements. Sample length is parallel to $[110]_{pc}$. Sample surface is parallel to $(001)_{pc}$. Thin dark lines are vertical $\{100\}_{pc}$ needle domains. $\{110\}_{pc}$ domain walls inclined at 45° to the surface are visible as bands of birefringent fringes.

from which M_1 , M_2 , J_1 , and J_2 can be extracted (l = distance between knife edges, w = width of sample, t = thickness of sample). A more detailed description of the DMA technique is given by Harrison and Redfern.¹

Two different types of experiment have been performed; temperature scans and dynamic force scans. In each temperature scan, F_S , F_D , and ω were held constant, while the temperature (T) was swept between room temperature and 300°C (encompassing the domain-freezing regime) at a rate of $3^\circ\text{C}/\text{min}$. Three sets of temperature scans were acquired using ratios of $F_S:F_D = 100:90$, $220:200$, and $500:450$ mN. Each set comprised several scans acquired with a range of frequencies from 0.01 to 32 Hz. To reduce the experimental noise in scans with frequencies below 0.1 Hz, three scans were performed under identical conditions and then aver-

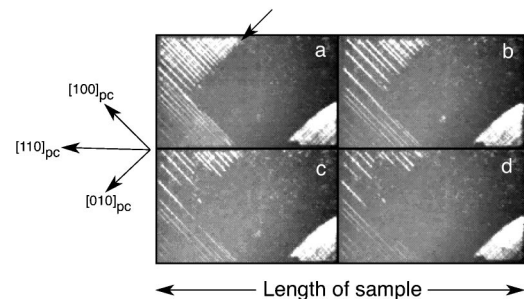


FIG. 2. *In situ* snapshots of the central region of the sample taken in reflected light at different stages of the dynamic force cycle (190°C , $200:180$ mN, 1 Hz). (a) A comb of $(010)_{pc}$ needle twins is visible in the upper and lower left corners. The central region, which appears blank, actually contains a comb of $(100)_{pc}$ needle twins, which becomes visible if the light source is moved (Ref. 15). The sharp termination of the $(010)_{pc}$ comb (indicated by the arrow) is caused by the presence of the $(100)_{pc}$ twins, which belong to an incompatible chevron orientation. Increasing the applied force causes retraction of the needles (b) and (c). There is a wide range of tip mobility within the domain-freezing regime, so that even at the maximum of the applied force (d) some needles remain unmoved. Movies of the twin response as a function of temperature are available online (Ref. 15).

aged. In each dynamic force scan, T and ω were held constant while F_D was swept between 50 and 500 mN at a rate of 10 mN/min. F_S was programmed to maintain a value of $1.1F_D$ at all times.

In situ optical observations of the twin microstructure and its variation during dynamical mechanical analysis at high temperature were made using a Perkin-Elmer DMA-7 equipped with a modified furnace and sample stage, designed to enable visual access to the bottom surface of the sample. The sample was illuminated from below using an optic-fiber light source and viewed in reflected light through a telescopic lens ($20\times$) attached to a black and white charge-coupled device camera. Data were recorded using a digital frame grabber operating at 25 frames per second (fps) and 320×240 pixel resolution. Typically, the sample contained several sets of differently oriented twin domains. Observations in reflected light permitted only one set of twins to be resolved at a time. Movement of the light source during the experiment was required to obtain images of all twins.

RESULTS

In situ optical observations

Movies illustrating the microstructural response at a range of different temperatures, frequencies, and applied forces are available on line.¹⁵ A sequence of snapshots illustrating the dominant mode of anelastic response is shown in Fig. 2. The snapshots show the central portion of the sample viewed at different stages of the dynamic force cycle. A comb of $(010)_{pc}$ needle twins is visible in the upper and lower left corners. The central portion of the sample, which appears blank, contains a comb of $(100)_{pc}$ needle twins belonging to a different chevron orientation. These twins become visible if the light source is rotated by 90° .¹⁵ Increasing the applied

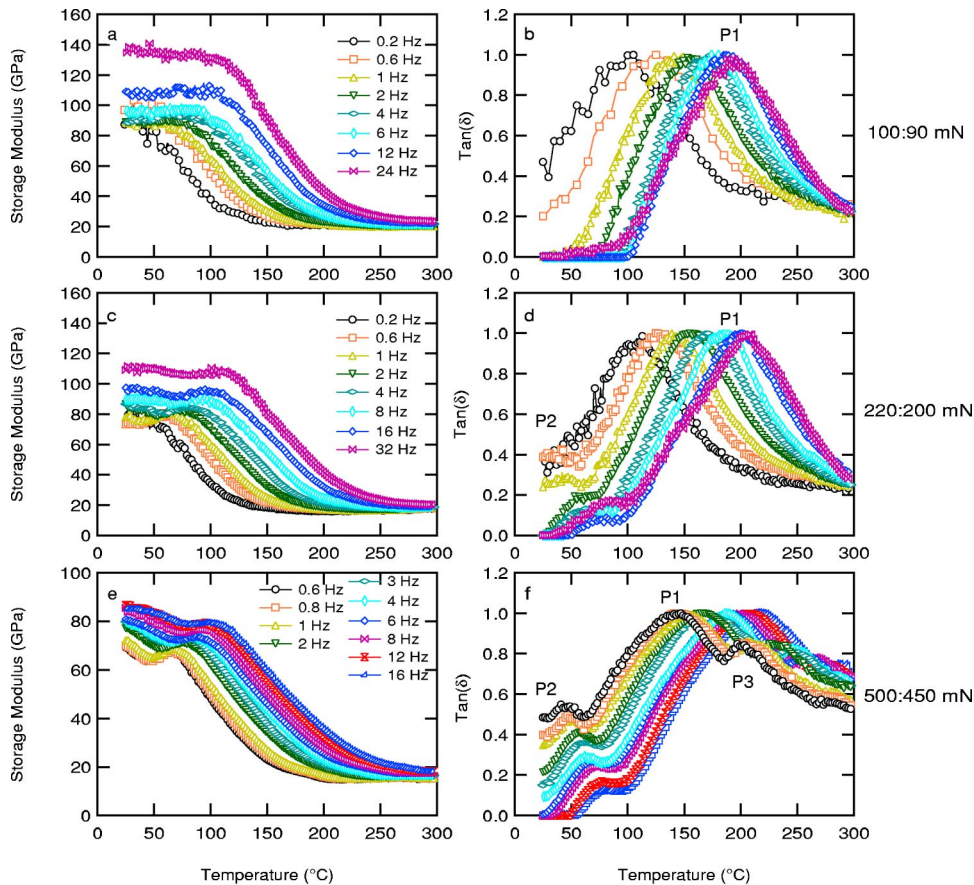


FIG. 3. (Color online) Storage modulus and $\tan \delta$ as function of temperature measured at a range of frequencies and applied forces (a), (b) 100:90, (c), (d) 220:200, and (e), (f) 500:450 mN. The relaxation spectrum contains a single peak at 100:90 mN (b), two peaks at 220:200 mN (d), and three peaks at 500:450 mN (f).

force causes retraction of needle tips toward the side of the sample. Decreasing the applied force causes the needle tips to advance back across the width of the sample. At low temperatures, the majority of needle tips are static, with a small number of tips undergoing small-amplitude displacements. With increasing temperature, needle tips are observed to escape their pinning sites and retract or advance rapidly until either (a) the next pinning site is reached, (b) the tip retracts to the side of the sample, or (c) a twin boundary from an orthogonal chevron orientation is encountered. Heating through the domain-freezing regime causes a steady increase in the ratio of mobile to static needles within a comb. At any given temperature there is a range of amplitudes of needle-tip displacement, with some needle tips remaining static, others oscillating between two discrete pinning points in the bulk, and others retracting and advancing across the entire width of the sample.

Ex situ observations in transmitted light under crossed polars reveal that the combs of $\{100\}_{pc}$ needle twins are intersected by bands of $\{110\}_{pc}$ walls inclined at 45° to the surface (Fig. 1). Resolving these walls in reflected light is difficult because the twin angle between adjacent domains is an order of magnitude smaller than for $\{100\}_{pc}$ walls.³ Our observations indicate that large-amplitude lateral displacements of $\{110\}_{pc}$ walls occur readily in regions free of $\{100\}_{pc}$ needles. During one measurement, where $\{100\}_{pc}$ needle domains were completely absent from the central region, the trace of a single $\{110\}_{pc}$ domain wall on the bottom surface of the sample was observed to track back and forth

over a distance of ~ 0.5 – 1 mm parallel to the sample length. Due to the three-point bend geometry, lateral displacement of the $\{110\}_{pc}$ walls occurs in opposite directions at the top and bottom surfaces, causing the wall to rotate out of its preferred crystallographic plane.¹ Diffraction evidence for this mode of anelastic response was obtained using stroboscopic x-ray diffraction DMA.³ When $\{100\}_{pc}$ needles are present, lateral displacements of the intersecting 45° $\{110\}_{pc}$ walls become easier once the needle tips have fully retracted to the side of the sample. At sufficiently high temperature and forces, therefore, the mode of anelastic response consists of a combination of advancement/retraction of $\{100\}_{pc}$ needles and displacement/rotation of $\{110\}_{pc}$ walls.

Frequency-dependent DMA

Temperature scans acquired using $F_S:F_D = 100:90$, 220:200, and 500:450 mN are presented in Fig. 3 in the form of storage modulus (M_1) and $\tan \delta$ (M_2/M_1) as a function of temperature. The results acquired at 100:90 mN and 24 Hz [pink curves (bow tie symbols) in Figs. 3(a) and 3(b)] display the typical characteristics of an anelastic relaxation process [Eq. (5)]. The storage modulus decreases smoothly from 140 GPa at room temperature (unrelaxed) to 20 GPa at 300 °C (relaxed). This relaxation is accompanied by a single peak in $\tan \delta$, labeled P1, which shifts to lower temperatures with decreasing frequency. At 220:200 mN [Figs. 3(c) and 3(d)], relaxation is preceded by a small increase in storage modulus and a second peak in $\tan \delta$, P2. P2 shifts to lower

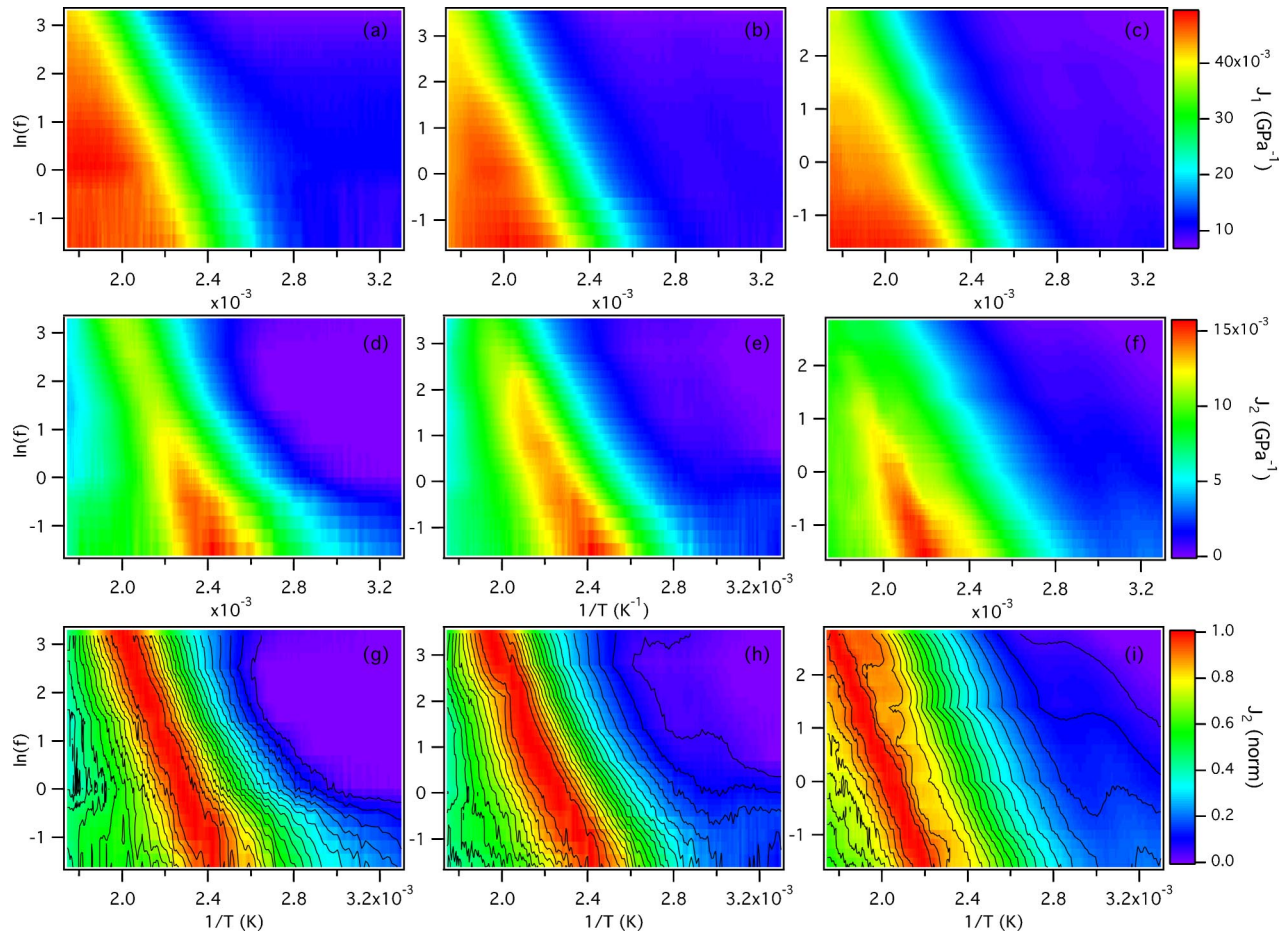


FIG. 4. (Color online) Two-dimensional plots of J_1 (a)–(c), J_2 (d)–(f), and normalized J_2 (g)–(i) as a function of $\ln(f)$ and $1/T$. Plots (a), (d), and (g) (left hand side) collected at 100:90 mN. Plots (b), (e), and (h) (central) collected at 220:200 mN. Plots (c), (f), and (i) (right hand side) collected at 500:450 mN. Contour lines added to normalized J_2 are equivalent to Arrhenius plots (g)–(i).

temperatures with decreasing frequency, although the magnitude of the shift is clearly less than that of $P1$. $P2$ is more pronounced at 500:450 mN [Figs. 3(e) and 3(f)], and a third peak $P3$ appears at high temperatures. Although $P3$ is not accompanied by a clear anomaly in storage modulus, it coincides with the temperature at which the fully relaxed storage modulus is reached (i.e., the high-temperature boundary of the domain-freezing regime).

The real and imaginary components of compliance, J_1 and J_2 , were calculated from the raw data in Fig. 3 using Eq. (4). The results are plotted as a function of $\ln(f)$ and $1/T$ for each of the three levels of applied force in Fig. 4. To obtain these plots, the raw data were projected onto a grid of $4N \times 271$ points, where N is the number of individual temperature scans acquired. The data were sampled at 271 points along the temperature axis (every 1°C between 30 and 300°C) and at $4N$ points along the $\ln(f)$ axis, using linear interpolation. The variation in J_1 at 100:90, 220:200, and 500:450 mN is shown in Figs. 4(a), 4(b), and 4(c), respectively. The corresponding variation in absolute and normalized J_2 is shown in Figs. 4(d)–4(f) and Figs. 4(g)–4(i), respectively. Contours added to Figs. 4(g)–4(i) trace lines of constant J_2 in $\ln(f)$ - $1/T$ space, and can be treated as Arrhenius plots [Eq. (7)]. For small and intermediate forces, con-

tours surrounding $P1$ are curved, with the curvature increasing with decreasing temperature and increasing frequency [top right corner of Figs. 4(g) and 4(h)]. The curvature of the contours is especially pronounced at 220:200 mN, where it is observable across the entire relaxation peak [Fig. 4(h)]. The origin of this curvature is explored below. For large forces, the contours are more linear, and an additional feature corresponding to $P2$ is visible [right hand side of Fig. 4(i)]. Arrhenius plots derived from the locus in $\ln(f)$ vs $1/T$ space of the maximum of $P1$ are shown in Fig. 5. Activation energies of 95, 85, and 86 kJ/mol were determined at 100:90, 220:200, and 500:450 mN, respectively (neglecting any curvature in the 100:90 and 220:200 mN data). The value of 86 kJ/mol at 500:450 mN agrees very well with the value of 84.1 kJ/mol determined at the same force level using a complementary analysis by Harrison and Redfern.¹ Such values have been attributed to the diffusion of oxygen vacancies.²⁰

The relaxation process can be followed as function of frequency at constant temperature by scanning vertically across the two-dimensional data of Fig. 4. Such constant- T data are presented in the form of Cole-Cole plots in Fig. 6 ($T = 160^\circ\text{C}$). Insets show J_1 and J_2 plotted individually as a function of $\ln(f)$. For a pure Debye relaxation [Eq. (5)] the

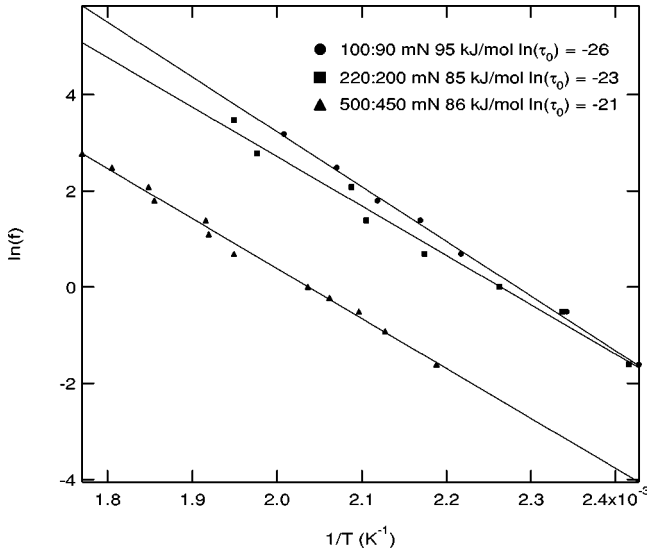


FIG. 5. Arrhenius plots of $\ln(f)$ vs $1/T$ obtained from the peak position of $P1$. Separate plots obtained for data collected at 100:90 (circles), 220:200 (squares), and 500:450 mN (triangles).

data should fall on a semicircle centered at $J_1 = J_U + \Delta J/2$ and $J_2 = 0$. In this case, however, the majority of data fall on the arc of a semicircle centered at $J_1 = J_U + \Delta J/2$ and $J_2 < 0$. Empirically, this behavior can be described using the Cole-Cole equation

$$J^*(\omega) = J_U + \frac{\Delta J}{1 + (i\omega\tau_{\text{Debye}})^\mu}, \quad (8)$$

where $0 < \mu < 1$. For $\mu = 1$, the equation for a pure Debye relaxation is recovered [Eq. (5)]. Decreasing μ simply broadens the spectrum relative to that of a pure Debye relaxation. Fits to the data using Eq. (8) are shown as the solid lines in Fig. 6. Excellent fits to J_2 versus $\ln(f)$ were obtained in all cases across the whole range of frequencies (see insets in Fig. 6). The fits to J_1 versus $\ln(f)$ were good at 500:450 mN [inset in Fig. 6(c)], but deviations were observed at low and high frequencies at 220:200 and 100:90 mN [insets in Figs. 6(a) and 6(b)]. These deviations are visible as a linear tail in the Cole-Cole plot at high frequency [dashed line in Fig. 6(a)]. The significance of this observation is discussed below.

Values of J_U , ΔJ , τ_{Debye} , and μ have been determined by fitting Eq. (8) to Cole-Cole plots extracted from Fig. 4 at a range of temperatures. The results for 220:200 mN are shown in Fig. 7. A linear fit to $\ln(\tau_{\text{Debye}})$ versus $1/T$ [Fig. 7(a)] yields an activation energy of 64 kJ/mol, significantly lower than that derived using the ‘‘peak-shift’’ method (Fig. 5). This discrepancy may be due to the curvature of the data in Fig. 5. The width of the relaxation spectrum varies as a function of temperature, leading to a systematic temperature dependence of μ [Fig. 7(b)].

Force-dependent DMA

The results of dynamic force scans are plotted as F_D versus u_D in Fig. 8 (all measurements performed at 1 Hz). The

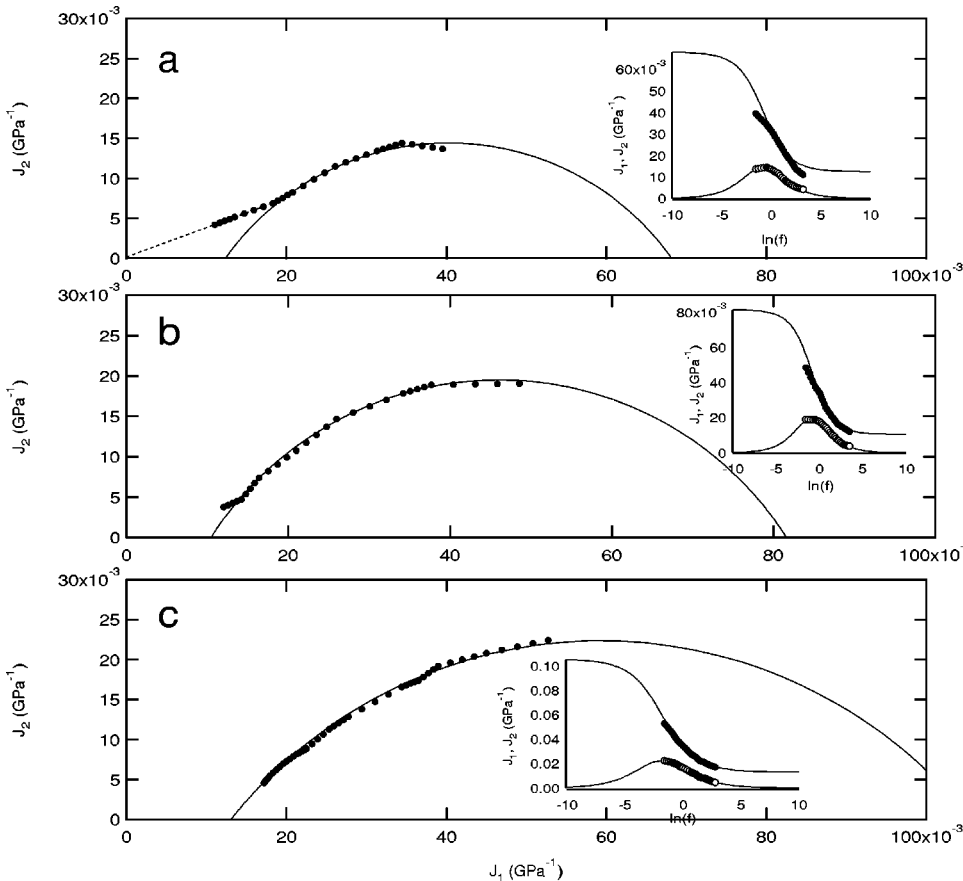


FIG. 6. Cole-Cole plots of $J_2(\omega)$ versus $J_1(\omega)$ for (a) 100:90, (b) 220:200, and (c) 500:450 mN. Data points obtained by scanning vertically across Fig. 4 at a temperature of 160 °C. Insets show J_1 (closed circles) and J_2 (open circles) as functions of $\ln(f)$. Solid lines are a fit to the data using the Cole-Cole equation [Eq. (8)].

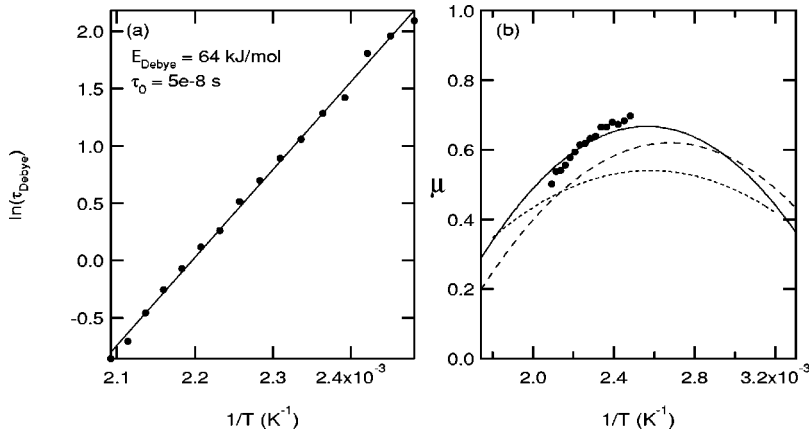


FIG. 7. (a) Arrhenius plot of $\ln(\tau_{\text{Debye}})$ versus $1/T$ determined by fitting Eq. (8) to Cole-Cole plots at a range of temperatures (see Fig. 6). (b) Broadening exponent μ versus $1/T$. Data points show values determined by fitting Eq. (8) to individual Cole-Cole plots extracted from the 220:200 mN data set at a range of temperatures. Solid curve shows the parabolic variation of μ versus $1/T$ determined by fitting the 220:200 mN data set at all temperatures and frequencies simultaneously. Dashed and dotted curves show the results of similar fits to the 100:90 and 500:450 mM data, respectively.

storage modulus is proportional to F_D/u_D [Eq. (7)]. The slope of the dashed line (i) corresponds to a storage modulus of 140 GPa [the highest value observed in Fig. 3(a)] and provides an estimate of the intrinsic mechanical response of the lattice. Nonlinearities in the observed mechanical response arise as different portions of the ferroelastic hysteresis loop are sampled at different temperatures and applied forces.^{16,17}

At room temperature, the initial slope of the dynamic force curve (ii) is much smaller than 140 GPa, indicating that some displacement of weakly pinned needle tips occurs under these conditions, as we have indeed observed optically. The initial slope decreases steadily to a value of ~ 20 GPa on heating to 200 °C, (iii–vii), consistent with the results of temperature scans at 100:90 mN [Fig. 3(a)]. Between 75 and 175 °C there is an abrupt increase in slope at forces greater than 200 mN (viii–xi). Such increases are usually attributed to saturation effects.¹ In the present case, saturation occurs when needle tips retract to the side of the sample, where they can no longer contribute to the macroscopic strain. It is unusual to observe saturation effects within the domain-freezing regime because a system that is partially relaxed cannot, by definition, be fully saturated. Partial saturation is possible, however, due to the varying mobility of individual needle tips. Under a certain applied force, only a fraction of the needle tips within a comb (i.e., the most weakly pinned) are mobile at low temperatures. These weakly pinned needle tips are able to retract fully at sufficiently high forces (causing the upturn in slope) while the more strongly pinned tips continue to relax normally (causing the decrease in initial slope with increasing temperature). Evidence for two partial saturation events can be seen in the measurements at 150 °C (x).

Saturation of weakly pinned needles is responsible for the low-temperature anomaly in the modulus and the $\tan \delta$ peak $P2$ [Figs. 3(c)–3(f)]. Partial saturation occurs at 75 °C and above. The increase in slope due to partial saturation causes the 75 °C curve to intersect the 50 °C curve at a dynamic force of 425 mN (note that such an intersection is physically possible only because the spontaneous strain at 50 °C is greater than that at 75 °C). Consequently, if measurements are made using dynamic forces greater than 425 mN, the modulus will increase with temperature between 50 and 75 °C, and then decrease again as the effect of partial satu-

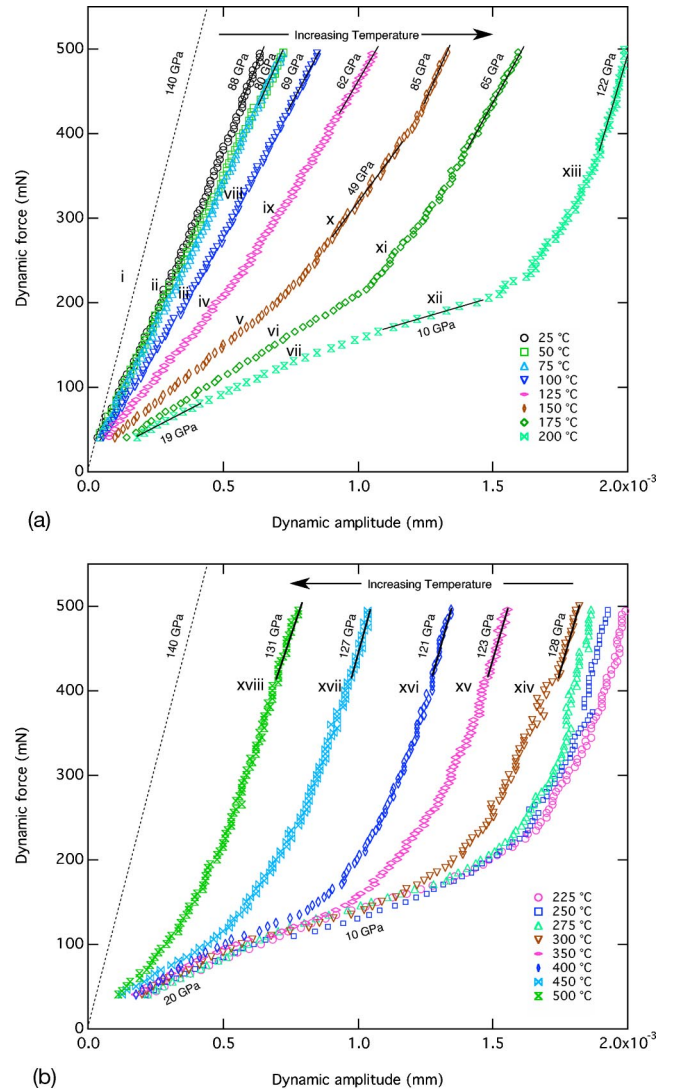


FIG. 8. (Color online) Dynamic force amplitude F_D versus dynamic deflection amplitude u_D at $f = 1$ Hz and temperatures from (a) room temperature to 200 and (b) 200 to 500 °C. Dashed line is a guide to the eye, showing a slope equivalent to 140 GPa (i.e., the intrinsic elastic response of the lattice). The slopes of selected linear sections are shown as annotations, with the section used to calculate the slope indicated by a short solid black line. Individual features of the curves are labeled i–xviii for referencing in the text.

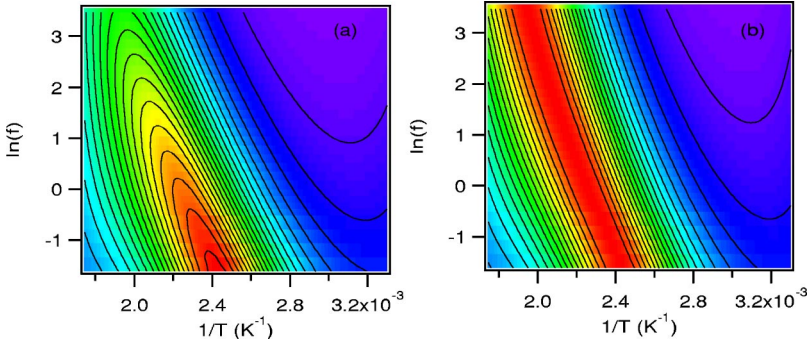


FIG. 9. Calculated variation in (a) J_2 and (b) normalized J_2 obtained by fitting the imaginary part of Eq. (8) to the 220:200 mN data at all temperatures and frequencies simultaneously. τ_{Debye} was fixed according to the linear fit in Fig. 7(a). The resulting parabolic temperature dependence of μ is plotted in Fig. 7(b). The calculated spectra can be compared directly to the observed spectra in Figs. 4(e) and 4(h).

ration is outweighed by further relaxation of the comb. This picture is confirmed by the temperature scan acquired at 500:450 mN, 1 Hz, which shows a pronounced maximum in modulus at 75 °C [Fig. 3(e)]. A less pronounced anomaly occurs at 75 °C in the 220:200 mN scan [Fig. 3(c)] and is completely absent in the 100:90 mN scan, where partial saturation does not occur [Fig. 3(e)].

Full saturation is achieved only toward the end of the domain-freezing regime, when all tips are able to retract simultaneously. This point is reached at temperatures greater than 200 °C and forces greater than 200 mN (xiii). At high forces, the slope of the dynamic force curve in the saturation regime approaches the intrinsic modulus of the lattice. This increase in slope, relative to that observed in the partial saturation regime, is responsible for the high-temperature modulus anomaly and $\tan \delta$ peak P3 [Figs. 3(e) and 3(f)]. Note also that the absolute deflection of the sample achieved in the saturation regime (xiv–xviii) decreases with increasing temperature [Fig. 8(b)]. This is simply due to the decrease in spontaneous strain on heating.

At 200 °C and above, the initial slope of the dynamic force curves is independent of temperature and has a value ~ 20 GPa. This corresponds to the fully relaxed modulus obtained via the needle advancement/retraction mechanism. At forces between 100 and 200 mN, however, the slope decreases by a factor of 2 (xii). This decrease may be explained by the change in mode of anelastic response to include the displacement/rotation of lamellar $45^\circ \{110\}_{\text{pc}}$ walls.³

DISCUSSION

Temperature dependence of μ

Key features of the relaxation spectra can be understood by referring to the temperature dependence of the broadening exponent μ [Fig. 7(b)]. Substituting Eq. (6) into Eq. (8), the two-dimensional data sets have been fitted at all temperatures and frequencies simultaneously. Values of τ_0 and E were fixed to those obtained from the data shown in Fig. 7(a). The variation of μ was assumed to be a polynomial function of $1/T$ (including constant, linear, quadratic, and one higher-order term, the exponent of which was varied in the fit). Calculated spectra, based on the results of fitting to the 220:200 mN data, agree very well with the observed data (Fig. 9). In particular, the decreasing height of the J_2 peak with increasing temperature and frequency [Figs. 4(d)–4(f)] and the curvature of the contours in normalized J_2 [Figs.

4(g) and 4(h)] are accurately reproduced. μ is found to be a parabolic function of $1/T$ (the high-order term refined to zero), as illustrated by the solid line in Fig. 7(b). The parabolic function passes close to the values of μ extracted from individual Cole-Cole plots [closed circles in Fig. 7(b)]. The whole-data fit extends the temperature range over which μ is reasonably constrained by the data and suggests that μ reaches a maximum value at ~ 120 °C.

The broadening exponent μ can be interpreted physically as a distribution of reduced relaxation times, $\rho(\tau_R)$, where $\tau_R = \tau / \tau_{\text{Debye}}$. Equation (5) then becomes

$$J^*(\omega) = J_U + \Delta J \int_0^\infty \frac{\rho(\tau_R) d\tau_R}{1 + i\omega \tau_R \tau_{\text{Debye}}}. \quad (9)$$

The distribution required to reproduce Eq. (8) from Eq. (9) is given by Leyderman and Qu:¹⁸

$$\rho(\tau_R) = \frac{\tau_R^{-(1-\mu)} \sin(\mu\pi) / \pi}{1 + \tau_R^{2\mu} + 2\tau_R^\mu \cos(\pi\mu)}, \quad (10)$$

which converges to a δ function for $\mu \rightarrow 1$. The distribution of relaxation times may reflect a distribution in activation energies, attempt frequencies, or both. Assuming that the distribution is in activation energy alone, and that each relaxor is independent of the others, we can relate the spread of relaxation times to a spread of effective activation energies via $E_{\text{eff}} = RT \ln(\tau_R) + E_{\text{Debye}}$. The first momentum $\tau_R \rho(\tau_R)$ is plotted versus E_{eff} in Fig. 10 for values of μ extracted from Cole-Cole plots at 130, 175, and 205 °C. The decrease in μ with increasing temperature translates to an increase in full width at half maximum of the activation-energy distribution from 9 kJ/mol at 130 °C to 21 kJ/mol at 205 °C. Widths in activation-energy distribution as large as 53 kJ/mol ($\mu \sim 0.3$) are predicted at 30 and 300 °C using the full-data fit [Fig. 7(b)].

We now discuss the physical origin of the distribution in Fig. 10. There are a number of factors contributing to the pinning of domain walls (e.g., spontaneous strain, domain-wall width, domain-wall density) that are intrinsic functions of temperature. The spatial width of domain walls in LaAlO_3 is ~ 20 Å at room temperature and increases with increasing temperature as $w(T) \propto 1/(T - T_c)$.¹⁰ Several authors have proposed point defects (e.g., oxygen vacancies) as pinning sites for ferroelastic domain walls.^{1,2,19,20} It is likely that domain walls become increasingly insensitive to point defects as their width increases, causing effective activation energies

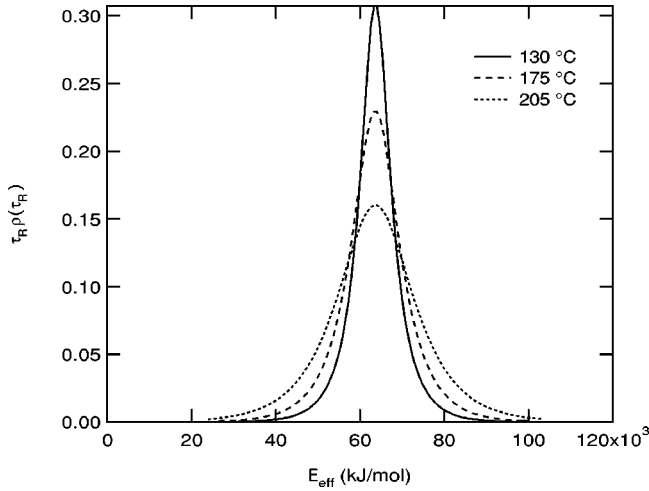


FIG. 10. Distribution of reduced relaxation times [Eq. (10)], plotted in the form of first momentum $\tau_R \rho(\tau_R)$ versus effective activation energy $E_{\text{eff}} = RT \ln(\tau_R) + E_{\text{Debye}}$. Curves are shown for three values of μ extracted from Cole-Cole plots at 130 (solid line), 175 (dashed line), and 205 °C (dotted line) [see Fig. 7(b)].

for domain-wall motion to decrease with increasing temperature. The temperature-dependent distribution of needle velocities and displacement amplitudes during the domain-freezing regime may contribute to the temperature-dependent distribution of activation energies through wall-wall interactions. Under specific circumstances, domain-wall densities increase with increasing temperature for a second-order transition as $n(T) \propto \exp(a|T - T_c|^{3/2}/T)$.²¹ This may lead to enhanced wall-wall interactions and larger activation energies. However, wall-wall interactions also depend on the square of the spontaneous strain,⁵ which decreases with increasing temperature as $e_s(T) \propto (T_c - T)$. Furthermore, geometric factors may be important $\{110\}_{\text{pc}}$ walls are likely to be more strongly pinned than $\{100\}_{\text{pc}}$ needles, due to the larger area of wall that is mobile. Hence, the increasing contribution from $\{110\}_{\text{pc}}$ walls on heating may cause a positive shift in the activation-energy distribution.

Dynamic transitions between different relaxation mechanisms

The dynamics of domain walls subjected to an alternating field in a random-pinning environment has recently been the subject of both theoretical^{16,17,22} and experimental²³ investigation in ferromagnetic materials. The results of such studies are equally applicable to the dynamics of ferroelastic domain walls subjected to alternating stress σ_D .²⁴ Four regimes of dynamic response are predicted to occur with increasing σ_D . For small stresses $\sigma_D < \sigma_\omega$, no macroscopic displacement of domain walls occurs at finite frequencies. Instead, segments of the wall undergo reversible relaxation between metastable states with close energies. This regime is characterized by a horizontal line in a Cole-Cole plot (i.e., constant but finite J_2).²³ For $\sigma_\omega < \sigma_D < \sigma_{t1}$, one enters a thermally activated creep regime. Macroscopic displacement of domain walls now occurs, characterized by a nonlinear relationship be-

tween domain-wall velocity and applied stress. This regime is characterized by a dynamic response function of the form²³

$$J^*(\omega) = J_U \left(1 + \frac{1}{(i\omega\tau)^\beta} \right), \quad (11)$$

$$J_1(\omega) = J_U [1 + \cos(\beta\pi/2)/(i\omega\tau)^\beta],$$

$$J_2(\omega) = J_U \sin(\beta\pi/2)/(i\omega\tau)^\beta,$$

where β is a phenomenological exponent, determined by the nonlinearity of the velocity-stress relationship. Equation (11) yields a straight line in a Cole-Cole plot with slope $J_2/(J_1 - J_U) = \tan(\pi\beta/2)$. For $\sigma_{t1} < \sigma_D < \sigma_{t2}$, one enters a domain-sliding regime characterized by large-amplitude viscous displacements of domain walls and a linear relationship between domain-wall velocity and applied stress. The dynamic depinning threshold σ_{t1} is equivalent to the critical depinning force F_D^{crit} , identified experimentally by Harrison and Redfern.¹ The domain-sliding regime becomes equivalent to the superelastic regime when the effects of restoring forces arising from wall-wall interactions and/or lattice compatibility strains are taken into account. In the presence of restoring forces, the domain-wall velocity decreases to zero as the equilibrium domain configuration (governed by the balance between applied and restoring forces) is approached. This leads to an exponential time dependence of the anelastic response [Eq. (1)] and a Debye-like semicircular dispersion in the Cole-Cole plot. The upper threshold σ_{t2} marks the stress at which domains are fully switched on a time scale equal to half the period of the applied stress. This is equivalent to the boundary between the superelastic and saturation regimes (Fig. 8). Note that σ_ω , σ_{t1} , and σ_{t2} are functions of both temperature and frequency, so that dynamic phase transitions between domain mobility mechanisms may be observed by traversing the relaxation spectrum at constant σ_D .

A transition between the thermally activated creep and domain-sliding regimes is clearly observable in Cole-Cole plots acquired at 160 °C and 100:90 mN [Fig. 6(a)]. At high frequencies, the Cole-Cole plot is linear, consistent with the thermally activated creep regime [Eq. (11)]. At lower frequencies, the domain-sliding regime is entered and the Cole-Cole plot becomes a depressed semicircle [Eq. (8)]. Cole-Cole plots acquired at 220:200 and 500:450 mN show

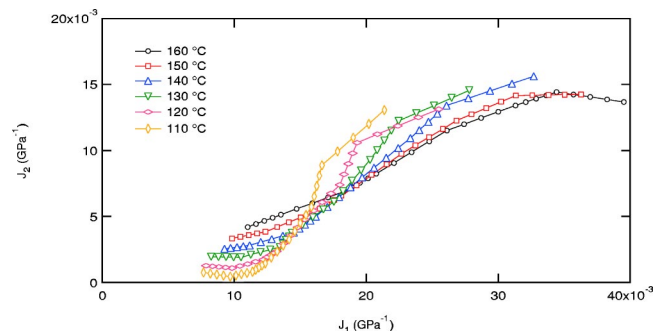


FIG. 11. Cole-Cole plots obtained at various temperatures using 100:90 mN force. Frequency range is 24 Hz (left hand side) to 0.2 Hz (right hand side).

suppression of the linear section, suggesting that $\sigma_D > \sigma_{t1}$ for both these measurements. At temperatures below 160 °C, there is some evidence that the initial slope of the Cole-Cole plots acquired at 100:90 mN decreases, suggesting a gradual transition between the thermally activated creep and domain-pinning regimes (Fig. 11). This observation is consistent with

the critical depinning of domain walls in LaAlO₃ observed by Harrison and Redfern.¹ A sharp depinning transition was observed in force scans at low temperatures, with the critical depinning force F_D^{crit} decreasing with increasing temperature. The depinning transition became smeared at high temperature, as the influence of thermally activated creep increased.

*Electronic address: rjh40@esc.cam.ac.uk

¹R. J. Harrison and S. A. T. Redfern, *Phys. Earth Planet. Inter.* **134**, 253 (2002).

²R. J. Harrison, S. A. T. Redfern, and J. Street, *Am. Mineral.* **88**, 574 (2003).

³R. J. Harrison, S. A. T. Redfern, A. Buckley, and E. K. H. Salje (unpublished).

⁴A. V. Kityk, W. Schranz, P. Sondergeld, D. Havlik, E. K. H. Salje, and J. F. Scott, *Phys. Rev. B* **61**, 946 (2000).

⁵Y. N. Wang, Y. N. Huang, H. M. Shen, and Z. F. Zhang, *J. Phys. IV* **6**, C8-505 (1996).

⁶E. M. Bourim, H. Tanaka, M. Gabbay, G. Fantozzi, and B. L. Cheng, *J. Appl. Phys.* **91**, 6662 (2002).

⁷A. S. Nowick and B. S. Berry, *Anelastic Relaxation in Crystalline Solids* (Academic, New York, 1972).

⁸S. Bueble, K. Knorr, E. Brecht, and W. Schmahl, *Surf. Sci.* **400**, 345 (1998).

⁹B. C. Chakoumakos, D. G. Schlom, M. Urbanik, and J. Luiane, *J. Appl. Phys.* **83**, 1979 (1998).

¹⁰J. Chrosch and E. K. H. Salje, *J. Appl. Phys.* **85**, 722 (1999).

¹¹H. Lehnert, H. Boysen, J. Schneider, F. Frey, D. Hohlwein, P. Radelli, and H. Ehrenberg, *Z. Kristallogr.* **215**, 536 (2000).

¹²C. J. Howard, B. J. Kennedy, and B. C. Chakoumakos, *J. Phys.: Condens. Matter* **12**, 349 (2000).

¹³S. A. Hayward, S. A. T. Redfern, and E. K. H. Salje, *J. Phys.: Condens. Matter* **14**, 10131 (2002).

¹⁴S. Bueble and W. W. Schmahl, *Mater. Struct.* **6**, 140 (1999).

¹⁵See EPAPS Document No. E-PRBMDO-69-029406 for a series of movies illustrating the microstructural response under various experimental conditions. A direct link to this document may be found in the online article's HTML reference section. The document may also be reached via the EPAPS homepage (<http://www.aip.org/pubservs/epaps.html>) or from <ftp.aip.org> in the directory /epaps/. See the EPAPS homepage for more information.

¹⁶I. F. Lyuksyutov, T. Nattermann, and V. Pokrovsky, *Phys. Rev. B* **59**, 4260 (1999).

¹⁷T. Nattermann, V. Pokrovsky, and V. M. Vinokur, *Phys. Rev. Lett.* **87**, 197005 (2001).

¹⁸A. Leyderman and S. Qu, *Phys. Rev. E* **62**, 3293 (2000).

¹⁹M. Calleja, M. T. Dove, and E. K. H. Salje, *J. Phys.: Condens. Matter* **15**, 2301 (2003).

²⁰C. Wang, Q. F. Fang, Y. Shi, and Z. G. Zhu, *Mater. Res. Bull.* **36**, 2657 (2001).

²¹E. K. H. Salje, *Phase Transitions in Ferroelastic and Coelastic Crystals* (Cambridge University Press, Cambridge, 1993).

²²A. Glatz, T. Nattermann, and V. Pokrovsky, *Phys. Rev. Lett.* **90**, 047201 (2003).

²³X. Chen, O. Sichel Schmidt, W. Kleemann, O. Petravic, Ch. Binek, J. B. Sousa, S. Cardoso, and P. P. Freitas, *Phys. Rev. Lett.* **89**, 137203 (2002).

²⁴D. Damjanovic, *Phys. Rev. B* **55**, R649 (1997).